RESEARCH ARTICLE

Key Points:
- Wave models overestimate wave height on opposing currents
- A modification to enhance dissipation is proposed
- The new term considerably improves the simulation of wave height and mean period

Current-induced dissipation in spectral wave models

H. Rapizo[1,2], A. V. Babanin[1,2] , D. Provis[3], and W. E. Rogers[4]

[1]Department of Infrastructure Engineering, University of Melbourne, Victoria, Australia, [2]Centre for Ocean Engineering, Science and Technology, Swinburne University of Technology, Victoria, Australia, [3]Cardno Ltd, Victoria, Australia, [4]Oceanography Division, Naval Research Laboratory, Stennis Space Center, Mississippi, USA

Abstract Despite many recent developments of the parameterization for wave dissipation in spectral models, it is evident that when waves propagate onto strong adverse currents the rate of energy dissipation is not properly estimated. The issue of current-induced dissipation is studied through a comprehensive data set in the tidal inlet of Port Phillip Heads, Australia. The wave parameters analyzed are significantly modulated by the tidal currents. Wave height in conditions of opposing currents (ebb tide) can reach twice the offshore value, whereas during coflowing currents (flood), it can be reduced to half. The wind-wave model SWAN is able to reproduce the tide-induced modulation of waves and the results show that the variation of currents is the dominant factor in modifying the wave field. In stationary simulations, the model provides an accurate representation of wave height for slack and flood tides. During ebb tides, wave energy is highly overestimated over the opposing current jet. None of the four parameterizations for wave dissipation tested performs satisfactorily. A modification to enhance dissipation as a function of the local currents is proposed. It consists of the addition of a factor that represents current-induced wave steepening and it is scaled by the ratio of spectral energy to the threshold breaking level. The new term asymptotes to the original form as the current in the wave direction tends to zero. The proposed modification considerably improves wave height and mean period in conditions of adverse currents, whereas the good model performance in coflowing currents is unaltered.

1. Introduction

Wave dissipation by breaking is of crucial importance in the evolution of wind-waves. In spectral models, this term has historically been based loosely on physics and treated simply as a tuning parameter to close the energy balance with the wind input term [*Babanin and van der Westhuysen*, 2008]. More recently, observed physical features of wave dissipation have been incorporated, tested, and validated in new parameterizations [*Ardhuin et al.*, 2010; *Babanin et al.*, 2010a; *Rogers et al.*, 2012]. The dissipation process has always been treated as a function of some form of wave steepness. If wave breaking is dependent on the wave steepness, the rate at which this occurs remains an open question. The larger dissipation rate over opposing currents observed by *Phillips* [1984] and associated with the rapid wave steepening induced by the mean flow in *Chawla and Kirby* [2002] suggests a nonlinear dependence of the dissipation on the spectral energy. However, *Ardhuin et al.* [2012] emphasize that there is no clear evidence of the advantage of nonlinear parameterization over linear forms and, in fact, linear models show a satisfactory performance at global scale. However, studies by *Ris and Holthuijsen* [1996], *van der Westhuysen* [2012], and *Ardhuin et al.* [2012] have provided convincing evidence that the rate of energy decay as currently represented in the parameterizations for wave dissipation is insufficient to simulate wave energy loss on adverse currents.

Spectral models operate on the radiative transfer equation (conservation of wave action) and are able to describe the evolution of the wave variance density $E(\sigma, \theta, \mathbf{x}, t)$ in space $\mathbf{x}$, time t, and spectral space, represented by radian frequency σ and direction θ, through the following general form:

$$\frac{d}{dt}\left(\frac{E}{\sigma}\right) = \frac{S}{\sigma},$$

(1)

where d/dt is the Lagrangian derivative which represents the rate of change of action E/σ following a wave packet in physical and spectral spaces. The use of action instead of energy is justified by the fact that the

former is conserved in conditions of an inhomogeneous current field [e.g., *Bretherton and Garret*, 1969]. In the right-hand side of equation (1), S comprises the contributions of nonconservative and nonlinear processes. These spectral source functions are generally subgrouped by positive atmospheric input S_{atm}, wave-wave nonlinear interactions S_{nl} and negative inputs from whitecapping dissipation S_{ds} and bottom friction S_{bf}, such that $S = S_{atm} + S_{nl} + S_{ds} + S_{bf}$.

Surface currents are included in the kinematic equations in the left-hand side of equation (1), by modifying the velocities of propagation which advect wave action in geographical and spectral spaces. It is also considered in the atmospheric input function S_{in} by balancing wind and current vectors. The key terms of nonlinear interactions and dissipation do not consider the background currents in their formulations. Nonlinear interactions, for example, is perturbed in the presence of a variable current field [*Waseda et al.*, 2015], which can affect the development of the spectral tail and slow the downshift of the spectral peak [*Rapizo et al.*, 2016]. Dissipation by breaking is calibrated to cases in the absence of currents [*Komen et al.*, 1984] and is clearly underestimated in conditions of strong negative currents [e.g., *Ris and Holthuijsen*, 1996]. However, the influence of currents on these processes has received little attention in the development of spectral models.

A number of studies have shown that improvements in wave modeling can be achieved through the development of the source functions in the right-hand side of (1) [e.g., *Donelan et al.*, 2006; *Ardhuin et al.*, 2010]. The source terms are traditionally calibrated and validated against known wave-growth experimental results in the time-space evolution of integral, spectral, and directional properties of the wave field. This approach is based on the attempt to reproduce empirical growth curves as a measure of the accuracy of the tested functions. Therefore, a term that is merely a tuning parameter of the other source quantities can simulate typical conditions well, but it is likely to produce erroneous results in nonstandard or complex situations [*Babanin and van der Westhuysen*, 2008]. As shown by previous studies [*Ris and Holthuijsen*, 1996; *van der Westhuysen*, 2012], one of these situations is wave modeling in the presence of strong currents. The parameterization of dissipation, which for decades was considered as a tuning parameter to achieve satisfactory performance, was identified by these authors as the one responsible for the significant overestimation of wave height when waves enter an opposing current field.

This paper investigates the performance of a spectral model in conditions of strong currents, opposing and following the direction of wave propagation. The issue of dissipation in adverse currents investigated in the aforementioned studies is revisited here by using a data set from Port Phillip Heads in Victoria, Australia, which is a tidal inlet where energetic waves propagate in the same direction as the tidal currents. This unique data set consists of several deployments of wave and current sensors along the axis of the entrance of Port Phillip Bay. This provides the ability to track the spatial evolution of waves as they propagate onto the tidal current jet. It is thus a rare opportunity to not only understand the interaction of waves with local currents but also to test the performance of wave models in such conditions. Different parameterizations for wave dissipation are validated including an alternative to enhance dissipation on negative current gradients proposed by *van der Westhuysen* [2012]. A new modification is proposed, which differs substantially from *van der Westhuysen* [2012] both conceptually and functionally.

The document is organized as follows. In section 2, a theoretical overview of three parameterizations for dissipation is presented including the default term of the Simulating Waves Nearshore (SWAN) model, which is the model used in this study. In section 2.1, the attempts to account for current-induced dissipation in existing terms are described and in section 2.1.1 an alternative modified term is proposed. This is followed by the analysis of the field data in section 3, which includes a description of the data set and models (section 3.1) and the results of the observed effects of currents on the wave field (section 3.2). In section 3.3, the default configuration of the wave model is qualitatively tested for nonstationary conditions. The performance of existing parameterizations for wave dissipation is quantitatively compared for all characteristic current conditions (slack, flood, and ebb tides) in section 3.4. In section 3.5, the implementation of the proposed term in the SWAN model is tested and validated. Finally, a discussion outlining the characteristics of the newly introduced factor and its essential differences from another alternative proposed in *van der Westhuysen* [2012] are given in section 4 followed by overall conclusions.

2. Parameterizations for Wave Dissipation

Three formulations for wave dissipation are briefly reviewed representing a general evolution of this term in spectral models to date. Since this study is performed in the framework of the SWAN model, the two first

parameterizations represent the two most widely used terms in SWAN, namely the *Komen et al.* [1984] term and the *van der Westhuysen et al.* [2007] formulation (hereafter KHH and WZB, respectively). The last function comprises a group of new generation terms introduced by *Ardhuin et al.* [2008] (extended to the directional form by *Ardhuin et al.* [2010]) and *Babanin et al.* [2010b], which was implemented in the SWAN model by *Rogers et al.* [2012] and will be referred to as RBW. Advantages and limitations of each term are discussed.

In spite of inconsistencies in the background theory, the term proposed by *Komen et al.* [1984] has been used as the standard dissipation term in wave models for decades. Justified by the "random pulse" theory of *Hasselmann* [1974], this function depends on the wave number k and other integral spectral parameters:

$$S_{ds\,KHH}(\sigma,\theta) = -C_{KHH}\,\tilde{\sigma}\,\frac{k}{\tilde{k}}\left(\frac{\tilde{s}}{\tilde{s}_{PM}}\right)^{q}E(\sigma,\theta), \tag{2}$$

where $\tilde{k} = [m_0^{-1}\int\int k^{-1/2}E(\sigma,\theta)\mathrm{d}\sigma\mathrm{d}\theta]^{-2}$ and $\tilde{\sigma} = [m_0^{-1}\int\int \sigma^{-1}E(\sigma,\theta)\mathrm{d}\sigma\mathrm{d}\theta]^{-1}$ are the mean wave number and mean frequency [*WAMDI Group*, 1988], respectively, in which m_0 is the total variance or integrated spectral energy. The overall wave steepness is $\tilde{s} = \tilde{k}\sqrt{m_0}$ and $\tilde{s}_{PM}$ is the corresponding mean steepness of the Pierson and Moskowitz spectrum for fully developed waves [*Pierson and Moskowitz*, 1964]. C_{KHH} and q are constants, where $q = 4$ in the SWAN default. Therefore, the dissipation is applied on the entire spectrum with no distinction between locally generated waves and swell and it strongly depends on the mean steepness by using a high value for the power coefficient q. Since this term was designed to close the balance with the other key terms of input (S_{in}) and nonlinear interactions (S_{nl}) such that $S_d = -S_{in} - S_{nl}$, its performance is quite satisfactory in standard situations of wind-wave growth. However, it has been shown to mistakenly decrease dissipation of swell with increasing steepness and overestimate wind-sea growth in the presence of swell [*Ardhuin et al.*, 2010].

Based on the experimental results of *Banner et al.* [2000] and *Babanin et al.* [2001], which found that there is no breaking if the dominant waves are below a certain threshold spectral steepness, *van der Westhuysen et al.* [2007] implemented a dissipation term consistent with some physical features of breaking waves

$$S_{ds\,WZB}(\sigma,\theta) = -C_{WZB}\left[\frac{B(k)}{B_r}\right]^{p/2}\sqrt{gk}\,E(\sigma,\theta), \tag{3}$$

where $B(k) = c_g k^3 E(\sigma)$ is the saturation spectrum following *Phillips* [1984], B_r is a constant which represents the saturation threshold, C_{WZB} is the dissipation constant and the variable p is a function of the inverse wave age u_*/c (in which u_* is the wind friction velocity and c is the wave phase velocity). This term was found to produce erroneous results when $p \approx 0$, with very large dissipation in oceanic scales. In order to overcome this issue, the WZB term is eventually replaced by the KHH formulation (2) for nonbreaking waves.

A new generation of dissipation terms were proposed independently by *Ardhuin et al.* [2008, 2010] and by *Babanin and Young* [2005] and *Babanin et al.* [2007, 2010b]. The formulations include a set of observed physical features, bringing consistency to the representation of the spectral dissipation process. The first feature is the threshold behavior of wave breaking, which was implemented in a different way than in the WZB term (3). A wave component now does not break unless its steepness exceeds a certain threshold value. The second characteristic is the so called cumulative effect, which accounts for the dissipation of the shorter waves induced by longer components. *Rogers et al.* [2012] unifies the new proposed terms into one formulation

$$S_{ds\,RBW}(\sigma,\theta) = T_1(\sigma,\theta) + T_2(\sigma,\theta), \tag{4}$$

where

$$\begin{cases} T_1(\sigma,\theta) = a_1 A(\sigma)\sigma\left[\dfrac{E(\sigma) - E_T(\sigma)}{\tilde{E}}\right]^{L}E(\sigma,\theta) \\[4mm] T_2(\sigma,\theta) = a_2\left[\displaystyle\int_{f_1}^{f_2}A(\sigma)\left(\dfrac{E(\sigma) - E_T(\sigma)}{\tilde{E}}\right)^{M}\mathrm{d}f\right]E(\sigma,\theta). \end{cases} \tag{5}$$

In the above equations, $A(f)$ is the directional width parameter [*Babanin and Soloviev*, 1998] and $\tilde{E}$ is the spectral normalization factor. When $\tilde{E} = E(\sigma)$ this term corresponds to *Babanin et al.* [2010b], whereas for $\tilde{E} = E_T(\sigma)$ it is equal to *Ardhuin et al.* [2008]. The threshold spectral density $E_T(\sigma)$ is defined as

$$E_T(\sigma) = \frac{2\pi B_{nt}}{A(\sigma)c_g k^3},\tag{6}$$

where $\sqrt{B_{nt}} = 0.035$ [*Babanin et al.*, 2007]. Wave dissipation is thus represented by a two-phase behavior specified by T_1 (inherent or local breaking) and T_2 (cumulative) [*Babanin and Young*, 2005]. The four free parameters to be calibrated are a_1, a_2, L, and M. *Rogers et al.* [2012] show that the choice of the normalization variable $\tilde{E}$ has an evident impact on (4). For $\tilde{E} = E_T(\sigma)$, the dependence of dissipation on $E(f)$ exhibits a rapid evolution of dissipation for $L, M > 1$ and the curve is characterized by a concave up form ("U"). Differently, when $\tilde{E} = E(\sigma)$ the dissipation is considerably less sensitive to L and M and the evolution curve has a concave down ("D"). The authors tested different values for the power coefficients. Because the UL4M4 form—i.e., $\tilde{E} = E_T(\sigma)$ (concave up), $L = 4$ and $M = 4$—performs better in the comparison with empirical growth curves this is the parameterization used in the present study. Furthermore, using L and $M = 4$ an expected larger dissipation within small space and time scales would favor this form when there is a rapid increase of wave energy such as in conditions of strong opposing currents [*Rogers et al.*, 2012].

2.1. Increased Dissipation Due to Currents

Spectral models significantly overestimate wave height for waves propagating onto adverse currents. This issue was first addressed by *Ris and Holthuijsen* [1996], who showed that the models poorly represent the wave dissipation process under these conditions. The performance of different parameterizations for wave dissipation on opposing currents, including those described in the previous section, is summarized in *Ardhuin et al.* [2012]. By modeling wave propagation on spatially varying currents using the flume experiments of *Lai et al.* [1989] the authors concluded that none of the models are fully satisfactory. The same experimental results were used by *Ris and Holthuijsen* [1996] to test the KHH whitecapping term. The insufficient breaking dissipation was further improved by the addition of a bore-based model adapted from *Battjes and Janssen* [1978] into the KHH formulation:

$$S_{ds\,RH}(\sigma,\theta) = -C_{RH}\,Q_b\,\tilde{\sigma}\,\frac{k}{\tilde{k}}\left(\frac{s_{MAX}}{\tilde{s}}\right)^2 E(\sigma,\theta),\tag{7}$$

where Q_b is the fraction of breaking waves and $s_{MAX}/\tilde{s}$ is a normalized maximum steepness, for which $s_{MAX} = 0.14$ (Miche's criterion) is the limiting steepness of an individual breaker, and $-C_{RH}$ is a constant. As a result of this criteria Q_b largely increases above $\tilde{s} = 0.08$ and thus it enhances wave dissipation of steep waves on opposing flows. However, the proposed model overestimates the dissipation of steep waves under growth conditions.

At this point, it is worth mentioning the results obtained by *Chawla and Kirby* [2002]. Through an extensive set of experiments, they proposed an empirical bulk dissipation formula, also based on the bore-based model of *Battjes and Janssen* [1978], that is able to simulate the dissipation rate near and at the blocking point. The formulation uses a probability of broken waves skewed toward larger wave heights and increased for steeper waves. The observations indicate that waves break at lower steepness than $s_{MAX} = 0.14$, applied by *Ris and Holthuijsen* [1996], due to the rapid increase of steepness on the opposing currents. Furthermore, the bore formulation of *Chawla and Kirby* [2002] includes the factor $\sqrt{gk}$, where d is the local water depth, which leads to a Doppler-shifted dependency on wave breaking. Despite the implicit inclusion of currents, the authors stress that the scaling parameters of the dissipation function are considerably different for depth-limited and current-limited breaking, which points out the necessity of relating these nondimensional parameters to local current and water depth.

Filipot and Ardhuin [2012] proposed a dissipation parameterization based on wave statistics that is not local in frequency, but related to a frequency window and adopting the bore model of *Chawla and Kirby* [2002] to estimate dissipation rate. The main objective was to unify deep and shallow water breaking into a seamless formulation. Although its performance on strong currents has not been tested, the proposed term includes the same coefficient $\sqrt{gk}$ to scale the rate of wave dissipation. However, it is not known how this term would perform in conditions of strong currents and if it would fall in the aforementioned limitation found in *Chawla and Kirby* [2002]. The nondimensional coefficient of the bore model (B in *Filipot and Ardhuin* [2012] and β in *Chawla and Kirby* [2002]) is adjusted by the factor $1/\tanh(kh)$. It is thus not conditioned by current-induced effects as suggested in *Chawla and Kirby* [2002] and, as recognized by the authors, their adjustment to B is somehow arbitrary so that breaking is more severe in shallower waters.

van der Westhuysen [2012] revisited the issue of wave dissipation on strong opposing currents in the SWAN model. In order to overcome the observed overestimation of wave height, *van der Westhuysen* [2012] proposed an addition to WZB [equation (3)], in the form

$$S_{ds\,WZB_C}(\sigma, \theta) = -C_{WZB_C} \max\left[\frac{c_\sigma(\sigma, \theta)}{\sigma}, 0\right] S_{ds\,WZB},$$ (8)

where $-C_{WZB_C} = 0.65$ is a constant calibrated using laboratory data, $S_{ds\,WZB}$ is defined in equation (3) and $c_\sigma(\sigma, \theta)/\sigma$ is the normalized propagation velocity in frequency space

$$c_\sigma = \frac{\partial \sigma}{\partial d}\left[\frac{\partial d}{\partial t} + \mathbf{U} \cdot \nabla d\right] - c_g \mathbf{k} \cdot \frac{\partial \mathbf{U}}{\partial s}.$$ (9)

By considering deep water conditions or a slowly varying depth d, equation (9) is reduced to $c_\sigma = -c_g \mathbf{k} \cdot \partial \mathbf{U}/\partial s$, which isolates current-induced effects. Therefore, the modification increases wave dissipation on negative current gradients (increasing opposing current or decreasing coflowing current speeds). The use of the maximum function in (8) excludes the effects of positive current gradients. *van der Westhuysen* [2012] tested the new formulation in the SWAN model implemented for the Amelander Zeegat tidal inlet, in a shallow flat region of the Wadden Sea, Netherlands. For wave sensors located on strong negative current gradients, the author found an improvement in the joint statistical quantities of H_s and mean period T_{m01}. However, the overall statistics considering all wave sensors deteriorated with the new dissipation term. This result was associated with the fact that the other source terms in the model were calibrated together with the original dissipation term. The parameterization 8 is hereafter denoted as WZB$_C$.

In the following section 2.1.1, the behavior of the term c_σ/σ applied in WZB$_C$ will be investigated in a simplified numerical model of wave propagation over a collinear and increasing negative current. We will also analyze its spatial distribution in opposing current conditions in the Port Phillip Heads in section 4.

2.1.1. Proposed Term

The results of *Chawla and Kirby* [2002] indicate that current-induced wave breaking and the consequent rate of energy decay are essentially different from depth-induced breaking. Among their final remarks, the importance of conditioning the coefficient parameter of the dissipation function to the local depth or currents is highlighted. Based on this reasoning and motivated by their results, an alternative method is proposed to enhance the dissipation rate on opposing currents.

Wave breaking dissipation is controlled by the wave steepness. The models formulated in section 2 depend on the spectral density $E(\sigma, \theta)$ and relate the dissipation to some form of wave steepness, either through integral parameters, as in KHH, or based on the saturation spectrum proposed by *Phillips* [1984] as applied in the WZB and RBW terms. For saturation-based functions, the breaking limit is treated in essentially different ways. In WZB, if a given saturation value is below the constant saturation threshold B_r, there is still a nonzero dissipation, whereas in RBW the threshold E_T is a cutoff level below which no breaking occurs.

Recognizing that the dissipation of waves is controlled by their steepness, we assume that the current-induced enhancement of dissipation can be related to the steepening of waves exclusively caused by the presence of currents. For simplicity, we can eliminate depth effects by considering waves in deep water (i.e., $kh \gg 1$). For a stationary current field that varies slowly in the wave direction, the conservation of action flux implies that [e.g., *Phillips*, 1977]

$$E\left(\frac{c}{2} + U_s\right)c = \frac{E_0 c_0^2}{2},$$ (10)

where the current speed U_s in the wave direction is given by $U_s = U_x \cos(\theta) + U_y \sin(\theta)$, E is the wave energy, c is the phase speed and the subscript "0" corresponds to the location where $U_s = 0$. In the above equation, nonconservative processes and nonlinear interactions are disregarded. From (10), it is straightforward to infer that

$$\frac{E}{E_0} = \frac{c_0^2}{2c(c/2 + U_s)}.$$ (11)

Equation (11) was originally derived by *Longuet-Higgins and Stewart* [1961] by considering the work done by the radiation stress against the current strain in the energy balance [*Longuet-Higgins and Stewart*, 1960].

For stationary current conditions, the *Doppler* effect gives $kU_s + \sigma = const.$ and thus the normalized variation of wave number can be represented by $k/k_0 = c_0/(c+U_s)$. From the normalized changes in wave number and energy (equation (11)), we can calculate the variations in wave steepness $\varepsilon = \sqrt{E}k$ as a function of the current speed U_s and the wave phase velocity c

$$\frac{\varepsilon}{\varepsilon_0} = \frac{1}{\sqrt{1+2U_s/c}\ (1+U_s/c)^3}.$$

(12)

Thus, the steepness is unchanged if the factor U_s/c is zero (or $U_s = 0$). A similar approach was used by *Huang et al.* [1972] and *Masson* [1996] to relate changes in the spectral energy to U_s/c_0. *Phillips* [1977] showed that the factor U_{MAX}/c is also determinant in the attenuation of waves after propagating through a region of opposing collinear currents. Another example is short waves superposed on longer waves, where the degree of saturation of the short wave components relative to the point where $U = 0$ is proportional to the velocity scale of the current variation U_c/c [*Phillips*, 1984]. Equation (12) has a singularity for $U_s = -\frac{1}{2}c$, where the wave energy becomes theoretically infinite, known as the "blocking velocity." At this point, breaking and reflection are mechanisms of energy releasing [e.g., *Moreira and Peregrine*, 2012].

Current-induced wave steepening is a function of $(1+U_s/c)^{-1}$. This term represents the ratio of intrinsic frequency to absolute frequency σ/ω resulting from the *Doppler* effect. In adverse currents ($U_s < 0$) we have that $\sigma/\omega > 1$, which implies steepening of waves and, consequently, the increase of breaking probability. This term may be conveniently written in terms of the absolute frequency, since $(1+U_s/c)^{-1} = (1-U_sk/\omega)$ and therefore (12) becomes

$$\frac{\varepsilon}{\varepsilon_0} = \frac{(1-U_sk/\omega)^3}{\sqrt{1+2U_s/c}}.$$

(13)

The factor U_sk/ω is a scale of the effects of the current on wave steepness. An interesting way to interpret this term is by expressing it as

$$\frac{U_sk}{\omega} = \frac{\omega-\sigma}{\omega} = \frac{\Delta\omega}{\omega}.$$

(14)

Based on (13) and (14) and recognizing that dissipation is closely linked to wave steepness, we assume that the increase in the dissipation rate on currents is proportional to the wave steepening induced by the current field. We can thus write that $S_{dsC} = f(\Delta\omega/\omega)S_{ds0}$, i.e., the dissipation S_{dsC} when currents are considered is modified by the normalized frequency shift as a scaling factor of the dissipation S_{ds0} in the absence of currents. This idea is substantially different from the assumption made in *van der Westhuysen* [2012], where the dissipation function is scaled by the normalized rate of change of wave steepness $\frac{d\varepsilon}{dt}/\varepsilon$, which is shown by the author to be directly proportional to the normalized propagation velocity (c_σ/σ) in σ space. As a consequence of the latter idea, the dissipation is a function of the mean current strain $\partial U_s/\partial s$ in the k-vector direction.

We can compare the behavior of both factors $\Delta\omega/\omega$ and c_σ/σ when waves propagate from quiescent water onto an adverse current by solving a simplified one-dimensional numerical model of the evolution of wave number $dk/dt = -k\partial U/\partial s$ under the assumption of conservation of wave action. Figure 1 shows the response of the two factors to current changes. The evolution of energy and steepness are shown in Figure 1a, (top). As the waves enter the opposing current, they steepen as a result of the increase of energy and also shortening of wavelength. The terms $\Delta\omega/\omega$ and c_σ/σ show different behaviors (Figure 1b). The latter increases rapidly as the current varies and decreases to 0 at the maximum opposing current speed. Term $\Delta\omega/\omega$ follows the wave steepness and thus is maximum along the largest adverse current values. Therefore, with the assumption of an enhanced dissipation as a function of $\Delta\omega/\omega$, the dissipation will increase when the current-induced wave steepening is considerable.

In order to account for the current-induced enhancement of wave dissipation, we apply the factor U_sk/ω responsible for wave steepening (equation (12)) as a dimensionless scale factor in the RBW source function [equation (4)], in the form

$$S_{ds\,RBW_C}(\sigma,\theta) = \left(1+a_3\max\left[-\frac{U_sk}{\omega},0\right]\frac{E(\sigma)}{E_T(\sigma)}\right)[T_1(\sigma,\theta)+T_2(\sigma,\theta)],$$

(15)

where $\omega = \sigma + kU_s$. We do not use the formulation for wave steepening (13) directly mainly because its value increases too rapidly toward higher frequencies, and to avoid singularities when $\sigma > -2U_sk$. The coefficient
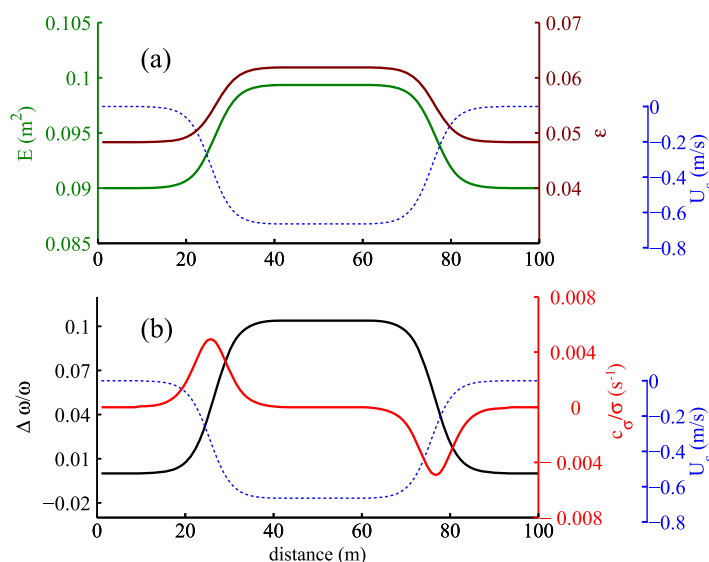
Figure 1. Results of a simplified numerical model of wave propagation onto a collinear adverse current: (a) evolution of energy (green line) and steepness ε (brown line) and (b) evolution of the normalized frequency shift $\Delta\omega/\omega = U_s k/\omega$ (black line) and normalized velocity of propagation in the frequency space c_σ/σ (red line). The current speed is shown by the blue dashed line.

a_3 is added to calibrate the strength of energy loss. The maximum function limits the effect of the additional factor to conditions of adverse currents $U_s < 0$ only. A few important characteristics of the proposed modification should be stressed. First, the factor $U_s k/\omega$ is scaled in spectral space by the ratio of energy to the saturation level $E(\sigma)/E_T(\sigma)$. By doing so, we obtain the increase in dissipation that is greater for frequencies at which the energy highly exceeds the breaking level. This approach is suitable for rapidly removing the overestimated energy when waves steepen on opposing currents. The term $U_s k/\omega$ itself affects more the dissipation of shorter components, however if $E(\sigma) < E_T(\sigma)$ there is no dissipation according to (4). Since the balance between local and cumulative breaking is not known for current-limited breaking, the enhancement factor is applied to both terms equally, thus keeping the ratio T_1/T_2 constant. Lastly, function (15) asymptotes to the original RBW term as $U_s \to 0$. The modified term proposed in (15) is denoted hereafter as RBW_C.

It should be mentioned that the factor $\sqrt{gk}$ used in *Chawla and Kirby* [2002] and *Filipot and Ardhuin* [2012] can be represented as $\omega(1-Uk/\omega)$ and, therefore, implicitly includes current effects. Therefore, it also accounts for current-induced steepening according to (13). The advantage of expressing the current effects explicitly as in (15) is that it is possible to calibrate the additional dissipation induced by opposing currents through coefficient a_3, keeping the asymptotic character of function (15).

3. Wave Dissipation in Tidal Inlets

Tidal inlets represent one of the most interesting environments to study wave-current interactions. The constriction of the tidal flow generates a current jet that can strongly affect the incoming waves. In Port Phillip Heads (PPH) (Figure 2), the energetic south/southwest swells generated in the Southern Ocean [*Rapizo et al.*, 2015b] and local wind-seas forced by south quadrant winds encounter a current field generated by a semidiurnal tidal regime. Currents are approximately collinear with the wave propagation, being characterized by opposing and coflowing jets during ebb and flood movements, respectively. The entrance is approximately 3.1 km wide. Two banks with a deep canyon are observed, with the Entrance Deep running across the main tidal flow. Two shallow banks are represented by the Nepean Bank, on the north, and the Rip Bank on the bass Strait side. Water depths on these banks are less than 20 m while the canyon has depths of close to 100 m.

During the ebb tide, the rapid steepening and breaking of waves is evident as can be seen from the aerial photograph shown in Figure 3. The picture shows a view toward the offshore direction (i.e., facing the incoming waves). A localized whitecap zone is clearly visible around the entrance, over the opposing current jet. The data used in this study were obtained at the positions shown by the blue markers in the map of Figure 2 (details are given in the next section). The spatial distribution of the point measurements provides a good coverage of the area of current-induced breaking, representing a unique opportunity to analyze the evolution of waves at different stages as they propagate along the tidal flow.
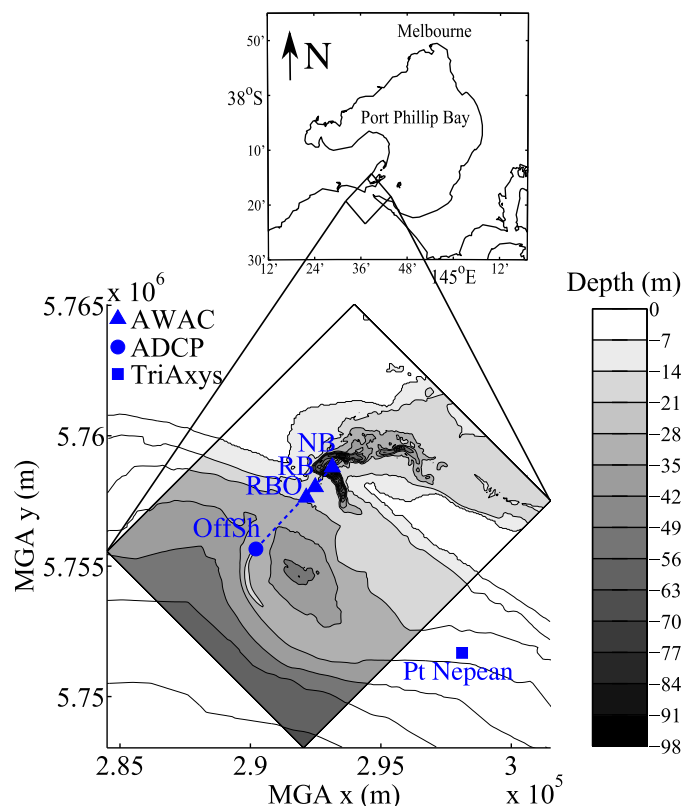
Figure 2. (top) Map of Port Phillip Bay and (bottom) bathymetry of Port Phillip Heads. The bottom grid is referenced to the Map Grid of Australia (MGA) metric system. The angled rectangle delimits the grid used in the SWAN model. Blue markers show position of wave and current sensors with their respective location names. The marker type corresponds to a specific sensor as shown in the legend.

3.1. Methods
3.1.1. Data Set

The field measurements were recorded by different sensors located in the surroundings of the PPH (Figure 2). Nortek AWAC (Acoustic Wave and Current) meters were moored in three different locations on a line (dashed blue line in the bottom) along the entrance, namely Rip Bank Outer (RBO), Rip Bank (RB), and Nepean Bank (NB). The AWAC provides the directional wave spectrum and the vertical profile of the currents in 20 depth cells. An ADCP (Acoustic Doppler Current Profiler) was located on a sand bank named Offshore Sandbar (OffSh) positioned further offshore approximately on the same line. It also provides the directional wave spectrum and current vertical profile. Finally, a TriAxys directional wave buoy is located southeast of PPH, at Point Nepean. Directional spectra are available from the AWACs and ADCP hourly and current profile every 20 min. Spectra from the TriAxys are available every 30 min. All spectra are based on 1024 samples at 1 Hz. As shown in previous studies [*Cardno*, 2007; *WL*, 2007] the four sensors along the entrance are highly affected by the tidal flow with a clear modulation of wave parameters at the tidal frequency, whereas at Point Nepean tide-induced effects are practically negligible. The wave parameters used in the analysis are represented by the significant wave height H_s, mean period T_{m01}, mean direction θ_m, and mean directional spreading σ_θ (see Appendix A for definitions).

In Figure 2, the angled rectangle delimits the domain of the wave model grid, which will be described in section 3.1.3. The shown bathymetry was obtained through a combination of different sources. In the vicinity of PPH, multibeam and Laser Airborne Depth Sounding (LADS) surveys provide high-resolution depth values (2 and 6 m horizontal spacing, respectively). The surveys used in this study are from 2008 (multibeam) and 2010 (LADS). In the distant regions (∼1 km from the Heads and outside the SWAN grid), the bathymetry data were obtained from a number of sources including single beam surveys (SBES) and navigation charts. All bathymetry data were reduced to Australian Height Datum (AHD). The local depth at OffSh, RBO, RB, and NB locations (along the entrance) are 19.7, 18.6, 18.8, and 17.15 m, respectively, while at Point Nepean (wave buoy) it is 28 m.

Four periods spanning approximately 15 days each were selected among 26 deployments between 2003 and 2012 based on the largest number of simultaneous measurements available. For modeling purposes, several cases of slack, flood, and ebb conditions were identified. Table 1 depicts the periods of the four events as well as the number of tidal cases considered. For the selection of slack tides, a condition of current speed smaller than 15% of the maximum speed for the period is imposed for all sensors. Consequently, the total number of slack cases (33) is comparatively small since the identification of slack current conditions is affected by the temporal resolution. However, the most important cases for our analysis are during flood and ebb currents, for which 86 and 88 cases were selected, respectively.

Figure 3. Aerial photograph of Port Phillip Heads showing wave breaking induced by ebb currents. The image was kindly provided by the Port of Melbourne Corporation.
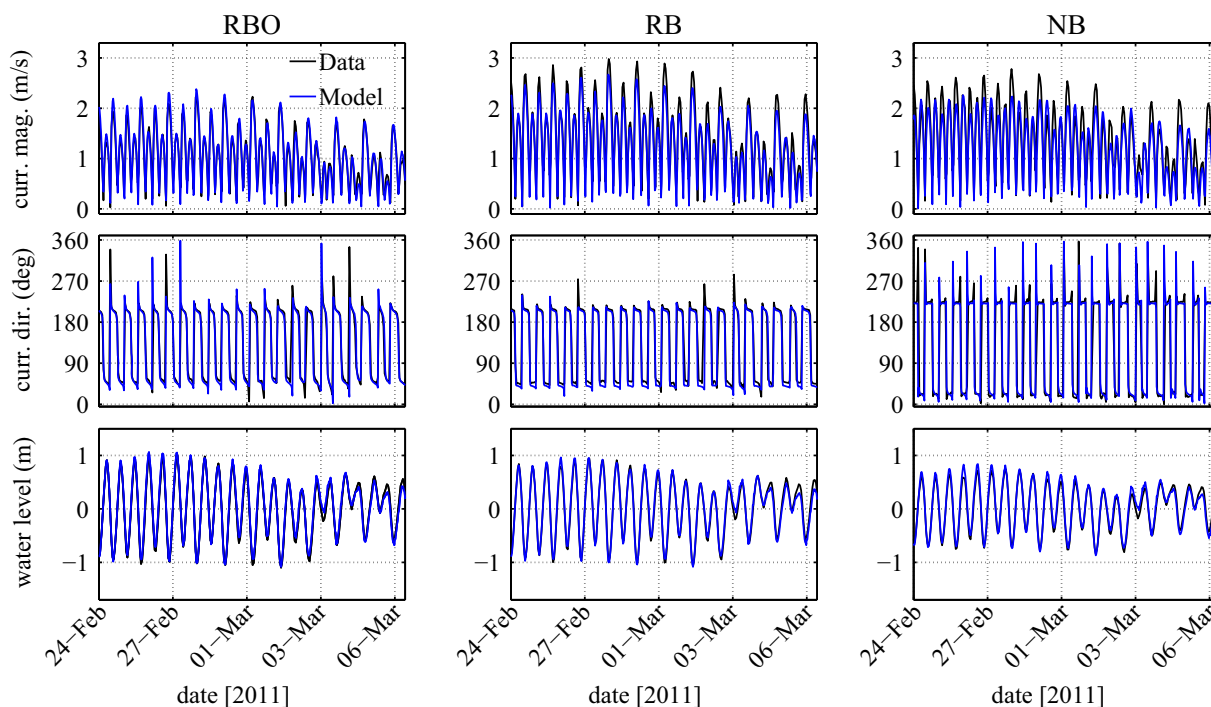
3.1.2. Hydrodynamic Model

The three-dimensional hydrodynamic Delft3D FLOW model was used to simulate the spatial fields of water level and three-dimensional currents in PPH. The model was configured with 20 m z-layers (vertical direction) with the top layer spanning $+2$ to -18 m AHD which includes the majority of the banks in the entrance but allows for definition of variable flow directions in the Entrance Deep, the canyon crossing the main flow direction between Nepean and Rip Banks. The 3-D z-layers approach proved to be able to accurately simulate the current field in the entrance [*Cardno*, 2007]. The model is forced by the sea level data measured at Lorne, approximately 75 km west of the entrance. The tidal signal was adjusted by minor changes to the major tidal constituents in order to correctly reproduce the tidal elevation recorded by the instruments in PPH. The model does not consider wind forcing or wave-induced currents. The top layer of the 3-D current field is taken as a two-dimensional spatial distribution, which is used as input to the wave model.

Figure 4 shows an example of the performance of the model in simulating water level and currents at the location of the three AWAC sensors along the entrance—RBO, RB, and NB. Model and data agree very well for water level and current direction ("curr. dir."). The modeled current magnitude ("curr. mag.") is highly accurate at the location of the first sensor (RBO) and it slightly

Table 1. Details of Selected Events Showing Period, Duration, and the Number of Individual Tidal Stages (Slack, Flood, and Ebb)

| | | | Number of Cases | | |
| | | Duration | | | |
Events	Period	(Days)	Slack	Flood	Ebb
1	2 Oct 2011 to 15 Oct 2011	14	7	20	22
2	16 Oct 2011 to 31 Oct 2011	15	8	24	23
3	3 Dec 2011 to 15 Dec 2011	13	12	20	21
4	2 Feb 2012 to 10 Mar 2012	15	6	22	22
Total		57	33	86	88

Figure 4. Performance of the hydrodynamic model DELFT3D FLOW at the location of the sensors in the bay entrance (RBO, RB, and NB) for the (top) current speed, (middle) current direction, and (bottom) water level.

underestimates the measurements during ebb tides (∼240° flow) at RB. For the NB sensor, the underestimation is more accentuated. It should be noted that NB has the deep canyon on three sides (see Figure 2), which is likely to affect the modeled outflow currents. During flood tides (∼40° direction) the model performs satisfactorily for all sensors. An extensive calibration and validation of this model is shown in *Cardno* [2007] including other sensors and deployments. Shipboard ADCP measurements along transects across the entrance also show good agreement with the modeled currents.

We assume a depth uniform current profile to be used in the wave model. The measured currents in the four different positions along the entrance revealed a very small vertical shear (not shown). The mean vertical shear during ebb currents (when measured current speed is largest) is ∼0.039 s at RB and ∼0.033 s at RBO. A relevant result to support the assumption of a homogeneous vertical distribution of the currents is found in *WL* [2007]. The study analyzed the same data set from Port Phillip Heads as used in our study. The implementation of a frequency-dependent effective current due to the depth-varying current profile using the approach of *Dingemans* [1997] (originally proposed in *Kirby and Chen* [1989]) in SWAN showed that the little stratification of the currents produce very small effects on waves.

3.1.3. Wave Model

The SWAN model [*Booij et al.*, 1999] version with open-source code contributions from the U.S. Naval Research Laboratory [*Rogers et al.*, 2012] was used to compute the evolution of the wave spectrum in the studied area. Since the calibration of the dissipation term is inherently coupled to the wind input, the parameterization for S_{in} must be chosen according to S_{ds}. When using the KHH parameterizations the wind input is represented by the default expression for exponential wave growth of *Komen et al.* [1984], whereas the WZB is combined with the wind input from *Yan* [1987]. For the RBW term and the modified term to account for the current-induced dissipation RBW$_C$, S_{in} is adapted from *Donelan et al.* [2006] (see *Rogers et al.* [2012] for details). In summary, S_{in} is modified by applying a constraint to the computed total stress: $\tau_{norm} \leq \tau_{tot} - \tau_v$, in which individual terms represent the normal, the total, and the viscous stresses, respectively. If this condition is not satisfied, the wind input is reduced by the factor $L_r(f) = \min[1, \exp(1 - U_{10})R]$, where U_{10} is the wind speed at 10 m height above the sea level and R is the reduction strength parameter. A drag coefficient $C_D \times 10^{-4} = 8.058 + 0.967U_{10} - 0.016U_{10}^2$ suitable for high wind speeds, proposed by *Hwang* [2011], is used. To run the model, the default physics for shallow water are activated with coefficient

for JONSWAP bottom friction S_{bf} of 0.038, discrete interaction approximation (DIA) scheme for four-wave nonlinear interactions S_{nl} [*Hasselmann et al.*, 1985], triad interactions S_{nl3} as described in *Eldeberky* [1996] and depth-induced breaking.

The model grid is represented by a regular grid of 267 × 212 nodes with resolution of 35 m and angled at 45° with respect to the vertical north-south axis (Figure 2). Upon inclining the grid, the lower boundary aligns with the entrance angle. Another considered aspect was the proximity of the active boundaries to the TriAxys buoy at Pt Nepean since the buoy data are used as the wave boundary condition in the model. The wind data from an anemometer installed on the lighthouse located inside the grid at ∼2 km west from the NB point (Pt Lonsdale) are used as the input wind field. Wind speed is converted to 10 m height by applying the drag coefficient proposed in *Hwang* [2011]. Water level and current fields are computed as described in section 3.1.2.

To assess the performance of the model, stationary and nonstationary simulations are performed. The latter are used to verify whether the model is capable of representing the modulation of the wave properties at the tidal frequency and to provide a sense of the behavior of the modeled waves at different tidal stages. Stationary simulations are the main focus of the present study. We identify the slack, flood, and ebb cases (section 3.1.1) and apply wind, wave, water level, and current conditions as described above. The stationary cases totaled 207 simulations—33 slack, 86 flood, and 88 ebb cases (see Table 1).

3.1.4. Statistics and Validation

The performance of the model is quantitatively validated for a specific wave parameter χ through the following statistics: Pierson's correlation coefficient r, normalized bias Nb, normalized root-mean-squared error $N\epsilon$ and scatter index SI, respectively defined as

$$r(\chi) = \frac{\sum(\chi_O - \bar{\chi}_O)(\chi_M - \bar{\chi}_M)}{\sqrt{\sum(\chi_O - \bar{\chi}_O)^2(\chi_M - \bar{\chi}_M)^2}},$$

$$\mathrm{Nb}(\chi) = \frac{\sum(\chi_O - \chi_M)}{\sum \chi_O},$$

$$\mathrm{N}\epsilon(\chi) = \sqrt{\frac{\sum(\chi_O - \chi_M)^2}{\sum \chi_O^2}},$$

$$\mathrm{SI}(\chi) = \frac{\sqrt{N^{-1}\sum(\chi_O - \chi_M)}}{N^{-1}\sum \chi_O},$$

(16)

where subscripts "O" and "M" correspond to the observed and modeled parameters, respectively, N is the number of analyzed samples and overbar is arithmetic average.

3.2. Tide-Induced Modulation of Waves

Time series of measured H_s, T_{m01}, θ_m, and σ_θ at the Rip Bank (RB) are shown in Figure 5. The series were recorded during event 3 (year 2011). The offshore measurements from the TriAxys buoy (Pt Nepean) are also shown for comparison (red line). The current speed in the NE-SW axis is plotted in the background (blue dashed line) so that positive values correspond to the coflowing currents (flood tide) and negative values to the opposing currents (ebb tide). This period was chosen due to the variety of conditions: shorter wind-waves from S/SE are dominant from 5 December to 8 December, followed by a longer SW swell. The wave height at the offshore buoy increases from less than 1 to 4.3 m. The most noticeable feature is that all wave parameters are clearly modulated at the tidal frequency at the entrance. The offshore wave measurements do not show any evident pattern of the tide-induced modulation.

During flood tides (coflowing currents), the wave energy at the entrance is decreased compared to that at the offshore buoy. In contrast, when the ebb currents oppose the direction of wave propagation, wave height is greater at the entrance. Considering the four events listed in Table 1, the measured H_s at the entrance reaches a maximum of 2.24 times the offshore value at ebb tide, whereas at flood tides wave height reduces with a factor up to 0.52. When waves propagate against a jet-like current, the increase of wave height can be produced by a combined effect of wavelength shortening and energy convergence. In
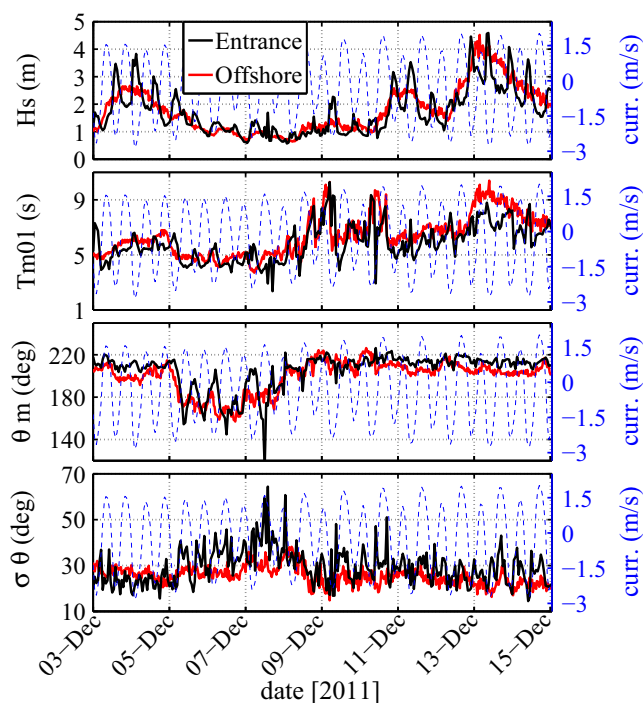
Figure 5. Time series of (from top to bottom): significant wave height H_s, mean period T_{m01}, mean direction θ_m, and mean directional spreading σ_θ measured by the Rip Bank sensor. Measured period corresponds to event 3. Currents projected on the NE-SW axis are plotted by the blue dashed lines for which the positive (negative) values correspond to the NE (SW) direction.

the former process, the wave number increases due to the strengthening of adverse currents and, based on the conservation of action E/σ, wave energy is augmented. Moreover, the convergence of wave rays due to the horizontal current gradients perpendicular to the k-vector concentrates the energy on the along-jet axis. The pattern of energy focusing/defocusing can be seen by means of the time series of mean directional spread (Figure 5, bottom). In general, the energy is focused in a narrow range of directions in adverse currents and it is more broadly distributed when waves propagate on a coflowing jet.

The variation of peak period T_p (not shown) is similar to that observed for mean period T_{m01}, with more high frequency oscillations due to the peak definition method. This result indicates that the current field is effectively unsteady and this is in agreement with previous studies for semidiurnal tide regimes [*Rapizo et al.*, 2015a; *Wolf and Prandle*, 1999]. The patterns of mean direction θ_m oscillation show that S/SE

waves possess a considerably greater deviation of direction compared to SW waves, where waves and currents are more aligned. Waves from S/SE enter the tidal jet obliquely and refract more sharply.

The analysis of the evolution of H_s and σ_θ along the entrance (Figure 6) is useful to understand wave energy variations. The oscillation of H_s is significant at the three sensors along the entrance. In the first two sensors (RBO and RB), the amplitude of variation of both parameters (H_s and σ_θ) are similar, increasing from RBO to
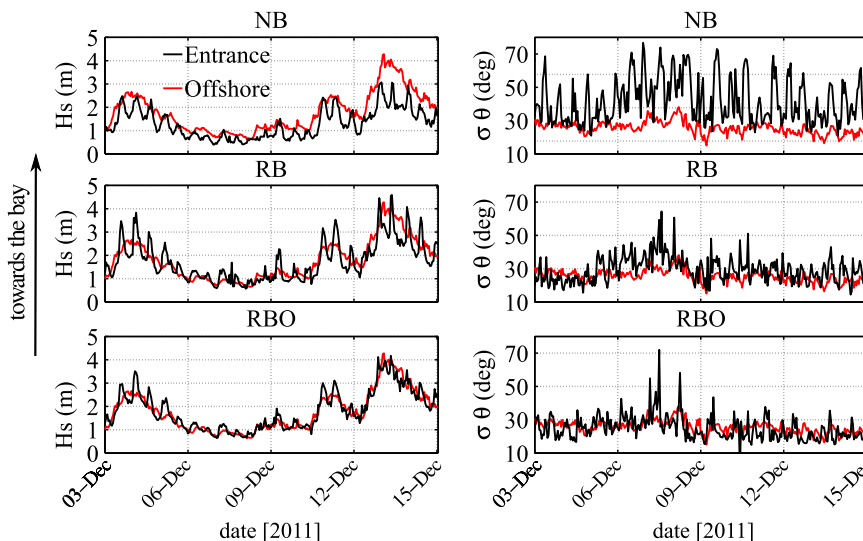

Figure 6. Time series of (left) H_s and (right) σ_θ for the sensors in the entrance region (RBO, RB, and NB). Measurement period corresponds to event 3.

RB as the waves propagate further into the current jet. Wave height reduces considerably at NB (last sensor), which is associated with an overall increase in mean spreading. It should be noted that, despite a similar local depth compared to the other locations, this sensor is positioned after the deep canyon (see Figure 2). The sharp gradient in bathymetry is probably a major factor in broadening the direction distribution of incoming waves as a consequence of the scattering of wave rays [*Ardhuin et al.*, 2003]. As a result, wave energy decreases. At this point, the oscillation of σ_θ is larger than at the other locations. This indicates that the opposing current jet constrains the wave energy in a narrow directional range, which avoids a strong energy divergence induced by the bathymetric gradient. On the other hand, the coflowing current contributes to the energy defocusing and, consequently, σ_θ shows a larger amplitude of oscillation. These results show that the tidal flow affects the directional distribution of waves in the entrance, which has a significant impact on the wave energy. However, it is likely that the overall reduction of H_s at NB is also influenced by the directional broadening and energy divergence due to bathymetric features. The observed wave modulations at RBO and RB are mostly controlled by the currents.

### 3.3. Relative Effects of Current and Water Level on Waves

The modulation of wave parameters at the tidal frequency is made clear in the previous sections. However, from the data analysis alone, it is not possible to determine the relative effect of water level and current variations on this process. Nonstationary simulations with SWAN (default parameterization KHH) are useful to identify the dominant process. Figure 7 shows the results of modeled H_s and T_{m01} for two different simulations: (1) with water level only (red lines) and (2) with water level and current fields (green line). The shown example corresponds to the RB location for the first event. The currents projected onto the SW-NE axis are plotted in the bottom. The two wave parameters are modulated almost entirely by the current field. The inclusion of water level creates essentially no modulation of energy or period. When currents are included the wave height oscillates with the tidal frequency with large amplitudes, in good agreement with the measurements. The mean period is reduced in the presence of currents, which is in a reasonably good agreement with observations.

An important feature can be observed in Figure 7. At the beginning and at the end of the series, H_s acquires larger mean values and the amplitude of the modulation is more prominent. The modeled wave height agrees well with the observations, but SWAN considerably overestimates the H_s values at ebb tides (negative current values) for the seven largest wave height peaks of the series. Based on the discussion in section 2.1 and the studies referenced therein, we can infer that the overprediction of the wave energy is caused by an underestimation of wave dissipation on opposing currents by the model.
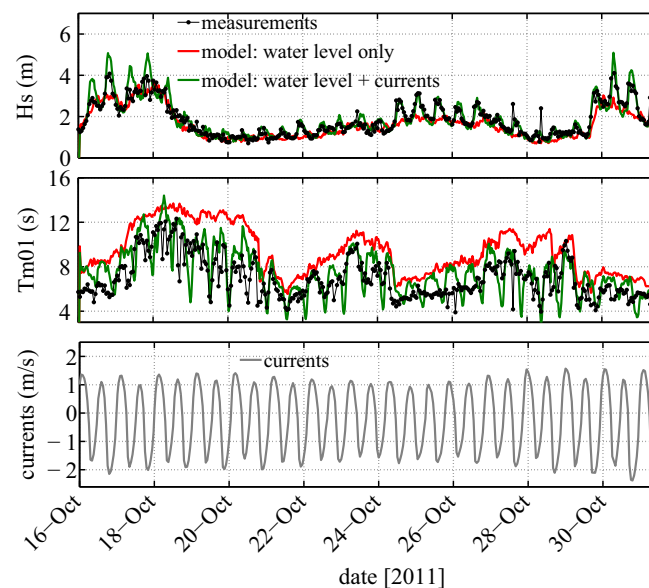
Figure 7. Time series of H_s and T_{m01} at RB for event 1. The observed values are shown by the black line with dots. The SWAN results including only water level and water level and currents are shown by the red and green lines, respectively. The current speed along the NE-SW axis is shown in the bottom.

Examples of typical spatial distributions of H_s during flood and ebb tides are shown in Figure 8. The current field provided by the hydrodynamic model (left) shows stronger currents in the bay entrance, with coflowing and opposing currents at flood and ebb tides, respectively. During the flood tide (Figure 8a), the wave energy decreases progressively as the waves propagate into the bay. For the ebb case (Figure 8b), the wave height field forms a zone localized over the strong tidal jet where the energy increases significantly. This process is a consequence of the combined effects of wavelength shortening and energy focusing as discussed in section 3.2. As the wave energy and steepness increase, the dissipation becomes more intense, which is confirmed by the aerial photography of Figure 3.
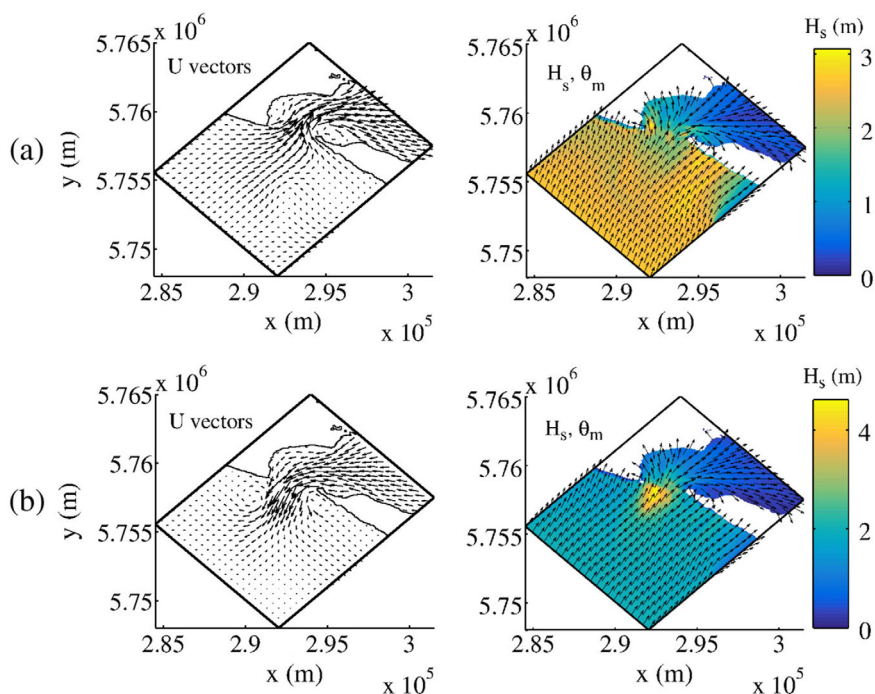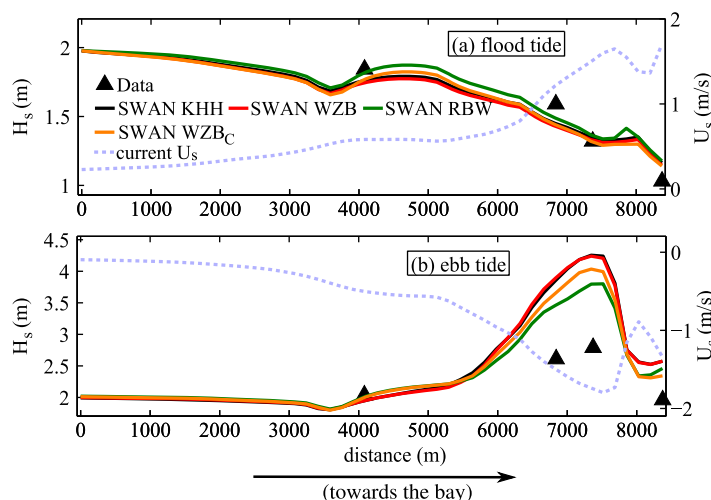
Figure 8. Typical spatial distributions of (left) current vectors from the hydrodynamic model and (right) H_s from SWAN default for (a) (top) flood tide and (b) (bottom) ebb tide.

### 3.4. Performance of Parameterizations for Wave Dissipation

Two important results were obtained in the previous section. The modeled wave height increases significantly over the ebb current jet and SWAN overestimates the wave energy in this region when the default dissipation term (KHH) is used. In this section, the performance of the dissipation terms KHH, WZB, RBW, and WZB_C described in section 2 is discussed for the stationary simulations at slack, flood, and ebb tides.

Figure 9 shows the evolution of measured and modeled H_s along the entrance for flood and ebb examples (a and b, respectively) from event 2. The modeled values correspond to a line starting at the boundary and containing the approximate location of the four sensors—OffSh, RBO, RB, and NB. The current speed in the mean wave direction U_s is also shown. The results of all dissipation functions are very similar for flood tide. A small increase in the wave height is observed at the first wave sensor (OffSh) due to wave shoaling on the offshore bank, where the models behave slightly differently. It is also observed smaller H_s values for the WZB_C term, which is a result of the increase of dissipation caused by the negative current gradients in the canyon region. In the ebb case, there is a clear difference between the RBW

Figure 9. Spatial evolution of H_s along the entrance for (a) flood and (b) ebb currents. Black triangles show observations. Model results using the KHH, WZB, RBW, and WZB_C parameterizations are shown by the black, red, green, and orange lines, respectively. The current speed U_s in the wave direction is shown by the blue dashed lines.
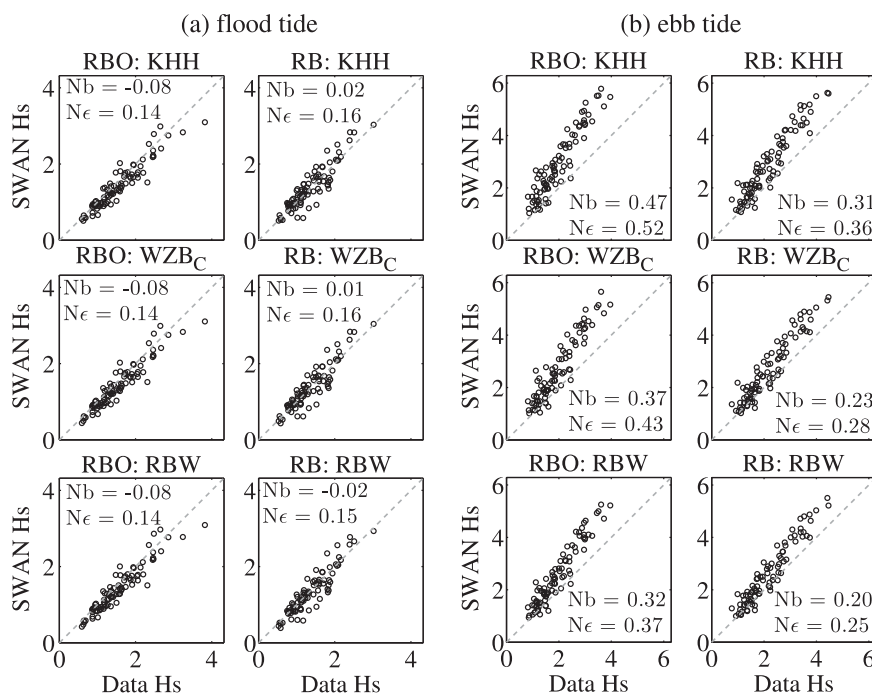
Figure 10. Scatterplots of wave height H_s for locations RBO and RB (over the current jet) for (a) flood and (b) ebb tides. Results correspond to (top) KHH, (middle) WZB$_C$, and (bottom) RBW parameterizations. Normalized bias Nb and root-mean-square error Nϵ are also shown.

and the other three parameterizations. For distance of around 5000 m from the boundary, all models produce similar results. As the opposing current strengthens, the KHH and WZB source functions perform similarly and the model strongly overestimates the wave energy at the two sensors on the current jet. Despite the larger dissipation, the WZB$_C$ function also significantly overestimates the wave height. This result will be discussed more thoroughly in section 4. The model predicts a more rapid dissipation of the energy when the RBW term is used. However, the shown example indicates that none of the terms performs satisfactorily when the waves face strong adverse currents.

The performance of different terms at the two locations where H_s is strongly overestimated (RBO and RB) is shown for flood and ebb cases by means of the scatterplots in Figure 10. We do not show the results for the WZB parameterization, since it performs very similarly to KHH. Normalized bias Nb and root-mean-square error Nϵ are given in each figure. As indicated in Figure 9, the modeled wave height agrees well with observations for flood currents (Figure 10a). Little difference is seen between the three parameterizations—KHH (top), WZB$_C$ (middle), and RBW (bottom)—with low biases and errors. However, it is clear that for ebb cases the overestimation of the wave energy is significant for the three parameterizations, being more accentuated when using the KHH model. Normalized bias reaches 0.47 (47%) for KHH. The use of WZB$_C$ improves the performance of the original WZB term (not shown here). The RBW model produces better results, although dissipation is still considerably underestimated.

Table 2 summarizes the statistical results for slack, flood, and ebb cases at all locations. We can see that the results for slack tide are similar to the flood cases, with a good performance of the model.

3.5. Validation of the Proposed Term

Four different values of the coefficient a_3 of equation (15), $a_3 = 1, 10, 30$ and 50, were tested. It should be noted that this study does not aim to precisely calibrate the coefficient a_3. For $a_3 = 50$, we observed an excessive dissipation and consequent underestimation of H_s for the last sensor (not shown here). We show the results for $a_3 = 30$, which improved the statistics for all analyzed locations. For a wave component with $T = 8$ s propagating from quiescent water to adverse currents, for example, at a point where $U_s = -2$ m/s, the factor $U_s k / \omega$ reaches the value of ~ 0.24 and, if we assume that $E(f_p)/E_T(f_p) = 1.5$ at this point, S_{ds} will increase approximately 11 times for $a_3 = 30$.

Table 2. Comparison of the Performance of the KHH, WZB, and RBW Terms for H_s[a]

	KHH			WZB$_C$			RBW		
	Slack	Flood	Ebb	Slack	Flood	Ebb	Slack	Flood	Ebb
OffSh									
r	0.93	0.93	0.92	0.94	0.93	0.93	0.94	0.93	0.94
Nb	0.029	0.093	0.121	0.026	0.089	0.129	0.050	0.115	0.130
Nϵ	0.149	0.170	0.189	0.147	0.169	0.191	0.151	0.186	0.195
SI	0.159	0.167	0.182	0.157	0.166	0.183	0.158	0.179	0.185
RBO									
r	0.96	0.94	0.94	0.96	0.95	0.94	0.96	0.95	0.95
Nb	−0.109	−0.076	0.473	−0.112	−0.081	0.368	−0.106	−0.084	0.316
Nϵ	0.146	0.142	0.525	0.148	0.142	0.432	0.141	0.144	0.373
SI	0.175	0.165	0.382	0.178	0.166	0.339	0.168	0.169	0.304
RB									
r	0.93	0.91	0.95	0.93	0.92	0.95	0.94	0.92	0.96
Nb	−0.022	0.023	0.313	−0.024	0.010	0.226	−0.030	−0.022	0.197
Nϵ	0.133	0.161	0.359	0.135	0.155	0.282	0.123	0.152	0.251
SI	0.146	0.168	0.295	0.148	0.164	0.248	0.137	0.165	0.226
NB									
r	0.94	0.89	0.92	0.94	0.93	0.93	0.95	0.93	0.93
Nb	0.145	0.230	0.247	0.141	0.171	0.113	0.096	0.151	0.141
Nϵ	0.195	0.284	0.285	0.191	0.231	0.183	0.158	0.217	0.203
SI	0.184	0.251	0.249	0.182	0.210	0.180	0.156	0.205	0.194

[a]All tidal cases (slack, flood, and ebb) and sensors (OffSh, RBO, RB, and NB) are shown. Statistical parameters are as follows: Pearson's correlation coefficient r, normalized bias Nb, normalized root-mean-square error Nϵ, and scatter index SI.

When the proposed current-dependent dissipation is considered the wave energy is significantly reduced over the current jet. Figure 11 shows an example of the evolution of H_s along the entrance. The original RBW term is compared with the new RBW$_C$ formulation. Measured and modeled spectra at RBO and RB (located on the strong currents) are shown in the bottom. This case illustrates the impact of the new dissipation function on the spectral energy. Incoming waves are represented by a bimodal system, with similar directions for low and high frequency peaks (205° and 217°, respectively). The difference between the terms does not affect the swell and SWAN provides a good representation of the energy level. However, wind-sea is highly overestimated by the RBW model. High frequencies are more affected by the opposing currents and the modeled energy increases rapidly. However, the measured wind-sea energy actually decreases, indicating a strong dissipation at those frequencies. With the inclusion of currents in the S_{ds} term, the
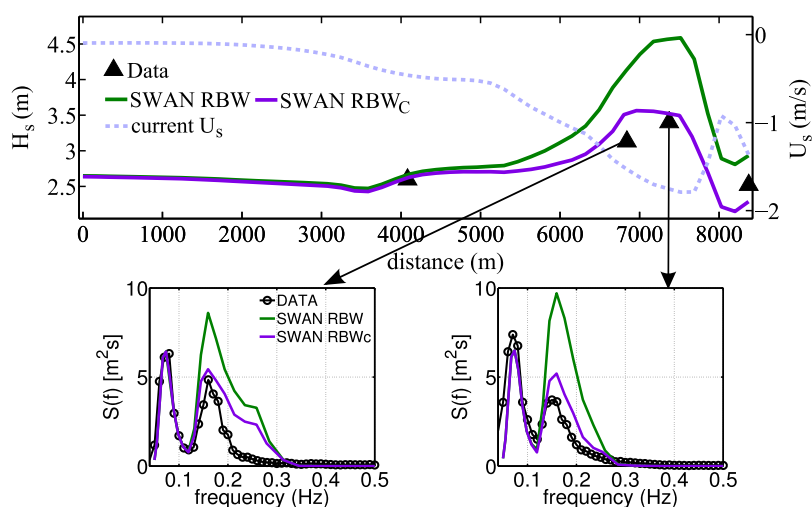

Figure 11. (top) Spatial evolution of H_s and wave spectra at (bottom left) RBO and (bottom right) RB. The black triangles (top) and black line with circles (bottom) show observations. Model results using the RBW and the modified RBW$_C$ terms are shown by the green and purple lines, respectively. The current speed U_s in the wave direction is shown by the blue dashed lines.

dissipation rate increases over the opposing currents and the energy level is better represented. It is noteworthy that both terms give identical results before the current strengthening. This happens because, despite the presence of a wind-sea (thus, a nonzero dissipation), the factor $U_s k/\omega \approx 0$ and hence S_{ds} is unaltered.

The larger dissipation at higher frequencies demonstrates two important features of the dissipation term. First, the inclusion of a threshold limit in the new generation terms, below which no dissipation occurs, produces little swell dissipation. The observations of swell-dominated cases show that wave energy increases over the adverse current jet and less dissipation can be noticed. For these cases, the differences between RBW and RBW_C are smaller. The second characteristic is related to the behavior of the factor $U_s k/\omega$ in the spectral domain. The wave number increases toward higher frequencies and the values of $U_s k/\omega$ become larger. Furthermore, the higher the peak frequency f_p the larger the ratio E/E_T. Consequently, the dissipation increases more for wind-sea-dominated waves, which are the most affected by the proposed modification.

The comparison between the original and proposed terms for all sensors is shown in the scatterplots in Figure 12. The blue rectangle highlights the two sensors located in the current jet, where H_s is overestimated. A significant improvement of the modeled energy is observed (a). As shown in Figure 11, the first location (OffSh, first column) is weakly affected by the new term since the currents are relatively slow in this region. The dissipation increases at RBO and RB (blue rectangle). The overestimation of H_s is largest at RBO for
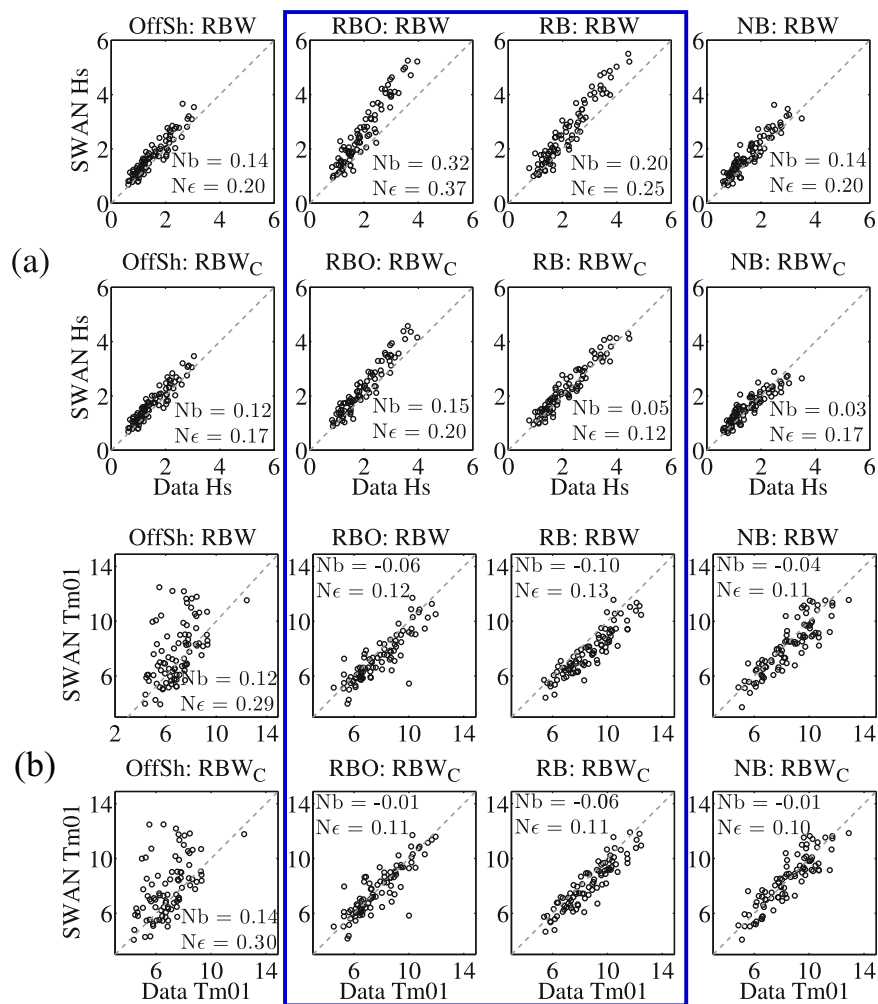
Figure 12. Scatterplots of (a) wave height H_s and (b) mean period T_{m01} for ebb tide cases. Results correspond to original RBW and current-dependent RBW_C (proposed) terms. Columns correspond to the various sensor locations. The normalized bias (Nb) and root-mean-square error (Nϵ) are also shown.

Table 3. Comparison Between the Original RBW Term and the Proposed Modification RBW$_C$ for H_s and T_{m01} for the Sensors in the Current Jet (RBO and RB Locations)[a]

	H_s		T_{m01}	
	RBW	RBW$_C$	RBW	RBW$_C$
RBO				
r	0.95	0.96	0.88	0.87
Nb	0.316	0.150	−0.061	−0.006
Nϵ	0.373	0.197	0.121	0.114
SI	0.304	0.187	0.132	0.119
RB				
r	0.96	0.96	0.92	0.92
Nb	0.197	0.045	−0.101	−0.059
Nϵ	0.251	0.119	0.126	0.105
SI	0.226	0.123	0.143	0.105

[a]Results correspond to ebb cases. Statistical parameters are as described in Table 2.

which Nb is reduced to half (from 0.32 to 0.15). At RB the modeled wave height now agrees very well with data and Nb is reduced from 0.20 to 0.05. Improved statistics are also seen for the last sensor (NB) although a small underestimation of the highest waves is observed. We remind the reader that this sensor is located after the canyon and the divergence of energy is the main factor in reducing wave height. Despite the smaller bias and error, H_s is still overestimated using RBW$_C$ at the RBO point.

The simulation of mean period T_{m01} also improves when the current-dependent term (Figure 12b) is applied. The effect of a larger dissipation at higher frequencies when RBW$_C$ is used can be observed by the increase of T_{m01}. The statistics for the three locations in the entrance are improved. In the OffSh position, the spectrum provided by the ADCP is noisy at high frequencies and T_{m01} is overestimated by the model, with high values of Nb and Nϵ for both terms. Table 3 compares the results for RBW and RBW$_C$ for the sensors on the current jet. Only ebb cases are shown, since the proposed modification does not affect the dissipation in conditions of coflowing currents.

4. Behavior of the Factor $\Delta\omega/\omega$

The enhancement of dissipation as proposed here is primarily controlled by the normalized *Doppler*-induced frequency shift $\Delta\omega/\omega = U_s k/\omega$. We find necessary to show and briefly discuss the behavior of the factor $\Delta\omega/\omega$ in the opposing current cases investigated. As shown in Figure 1, this term increases as waves steepen on adverse currents. From the field data, we observed that the region of stronger currents is associated with the overestimation of the wave height by the SWAN model. Therefore, it is expected that the values of $\Delta\omega/\omega$ reach a maximum around the entrance, where the strongest currents are measured.

It is noteworthy that improvements in simulations with currents were also achieved in *van der Westhuysen et al.* [2012] (WZB$_C$ term) in which dissipation increases as a function of c_σ/σ so that it is essentially
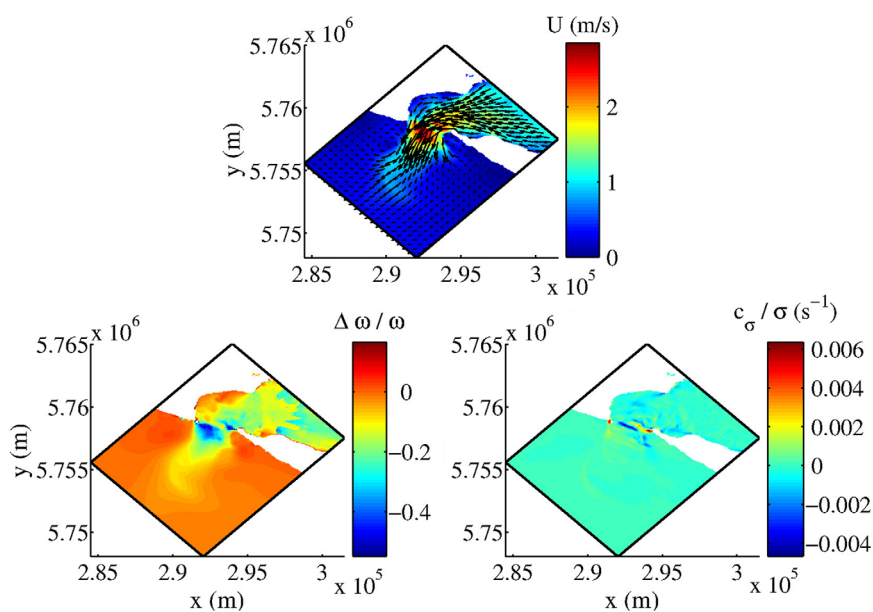
Figure 13. Comparison between the spatial distribution of factors (bottom left) $\Delta\omega/\omega$ and (bottom right) c_σ/σ at the spectral peak in an ebb current field of event 1. (top) Current vectors and speed (color scale) for the case considered.

controlled by the current strain $\partial \mathbf{U}/\partial s$ in the wave direction. Figure 13 shows the comparison between the spatial distribution of these two terms—c_σ/σ (applied in WZB$_C$) and $\Delta\omega/\omega$ (proposed in this study)—as calculated by SWAN for an ebb tide case of event 1. The values correspond to the spectral peak of incoming waves with peak period $T_p = 7$ s. In the field cases tested here, the largest values of c_σ/σ are 2 orders of magnitude smaller than $\Delta\omega/\omega$. There is no clear pattern of the c_σ increase as the waves approach the inlet and where the wave height is overestimated. In contrast, the normalized frequency shift becomes larger in the entrance region. This term is controlled by the ratio between the current and wave phase velocities and it increases as the waves slow when they enter the adverse current region. The behavior observed in Figure 13 is analogous to the result from the simplified model shown in Figure 1. Since $\Delta\omega/\omega$ is related to the degree of wave steepening induced by the opposing current, it enhances dissipation in the entrance, where stronger currents are observed.

5. Conclusions

The data analysis shows that the wave properties are strongly modulated by the tidal currents in Port Phillips Heads. Waves propagate approximately aligned with the mean currents in the entrance region and they are modified differently depending on the tidal stage. At flood tides, the waves lengthen and lose energy. Over the ebb currents wavelength shortens and the energy increases up to the maximum current speed. The observations of the mean directional spreading suggest that directional broadening and narrowing of waves are tightly related to changes in H_s, indicating that wave divergence and convergence during flood and ebb currents, respectively, are significant in the modulation of wave energy.

The spectral model SWAN is able to reproduce the wave modulation well and the results show that currents are the main cause of the semidiurnal oscillation pattern. However, the model significantly overestimates wave height when waves propagate over strong adverse currents. This is associated with a poor representation of the dissipation process in such conditions. Four parameterizations for the dissipation term are tested: the *Komen et al.* [1984] term (KHH), the *van der Westhuysen et al.* [2007] formulation (WZB) and its modified version WZB$_C$ [*van der Westhuysen*, 2012] and the term presented in *Rogers et al.* [2012] (RBW), with $\tilde{E}=E_T(f)$ and power coefficients $L, M=4$. The model agrees well with observations for slack (no current) and flood (coflowing currents) tidal stages. None of the terms performs satisfactorily for ebb tides (opposing current), with a better performance of RBW.

The inclusion of a current-dependent factor in the RBW term is tested. The new factor is a function of the normalized current-induced frequency shift $\Delta\omega/\omega=U_s k/\omega$ and thus it is directly dependent on the local currents in the k-vector direction. The following features of the proposed modification should be highlighted:

1. Since the dimensionless factor $U_s k/\omega$ controls current-induced changes in wave steepness (see equation (13)), the dissipation increases in areas where the waves propagate over opposing currents.
2. A multiplication factor in the form $[1-U_s k/\omega(E/E_T)]$ is used so that the modified function asymptotes to the original term RBW as $U_s \to 0$.
3. The dissipation is not modified if the current speed is 0 ($|\mathbf{U}|=0$) or if the current vector is perpendicular to the wave number vector (i.e., $\mathbf{U} \perp \mathbf{k}$).
4. Based on observations of the spectrum in the region of H_s overestimation, we add the scale factor E/E_T. This term strengthens dissipation at frequencies where the spectral energy is much larger than the threshold level.

The modified term improves the model results substantially in conditions of adverse currents. Its inclusion has no influence on the good performance of the model in conditions of coflowing currents. It should be stressed that the current-dependent term proposed in this study was tested for a few values for the coefficient a_3 in (15). The dissipation is not very sensitive to variations in a_3 and it was observed that changes of a_3 of $O(10)$ start to produce considerable differences. In a future work, the proposed modification for wave dissipation will be tested in a variety of conditions by changing mainly the spatial scale of wave steepening over the opposing currents. Laboratory results will be included in order to bring a more precise calibration of the coefficient a_3.

Appendix A: Definition of Wave Parameters

The wave parameters used in the analysis are obtained through the wave spectrum. Peak period $T_p = 1/f_p$ and peak wave number $k_p = 2\pi/\lambda_p$, where f_p and λ_p are the frequency and wavelength at the spectral peak, respectively. The definition of other parameters are based on the spectral moments $m_n = \int_0^\infty f^n S(f) \, df$, where n is the moment order and $S(f)$ is the variance density spectrum of the surface elevation. The significant wave height is approximated as the zeroth-order moment wave height

$$H_s \approx H_{m0} = 4\sqrt{m_0}. \tag{A1}$$

The mean period is

$$T_{m01} = \frac{m_0}{m_1}. \tag{A2}$$

The mean direction and the mean directional spreading are based on the definition of *Kuik et al.* [1988] of principal wave direction $\theta_0(f)$ and directional width $\sigma_\theta(f)$, respectively

$$\theta_m = \arctan\left[\frac{\bar{b}_1}{\bar{a}_1}\right], \tag{A3}$$

$$\bar{\sigma}_\theta = \sqrt{2[1 - (\bar{a}_1^2 + \bar{b}_1^2)^{1/2}]}, \tag{A4}$$

where

$$\bar{a}_1 = \frac{1}{m_0} \int_0^\infty a_1(f)S(f) \, df$$
$$\bar{b}_1 = \frac{1}{m_0} \int_0^\infty b_1(f)S(f) \, df, \tag{A5}$$

where a_1 and b_1 are the first two Fourier coefficients. For simplicity, the mean directional spreading is denoted by σ_θ (without overbar) throughout the text.

References

Ardhuin, F., W. C. O'Reilly, T. H. C. Herbers, and P. F. Jessen (2003), Swell transformation across the continental shelf. Part I: Attenuation and directional broadening, *J. Phys. Oceanogr.*, *33*, 1921–1939.

Ardhuin, F., F. Collard, B. Chapron, P. Queffeulou, J.-F. Filipot, and M. Hamon (2008), Spectral wave dissipation based on observations: A global validation, in *Proceedings of the Chinese-German Joint Symposium on Hydraulics and Ocean Engineering*, pp. 391–400, Darmstadt, Germany. [Available at http://www.comc.ncku.edu.tw/joint/joint2008/papers/69.pdf.]

Ardhuin, F., et al. (2010), Semiempirical dissipation source functions for ocean waves: Part I: Definition, calibration, and validation, *J. Phys. Oceanogr.*, *40*, 1917–1941.

Ardhuin, F., A. Roland, F. Dumas, A. Bennis, A. Sentchev, P. Forget, J. Wolf, F. Girard, P. Osuna, and M. Benoit (2012), Numerical wave modeling in conditions with strong currents: Dissipation, refraction, and relative wind, *J. Phys. Oceanogr.*, *42*, 2101–2120.

Babanin, A. V., and Y. P. Soloviev (1998), Variability of directional spectra of wind-generated waves, studied by means of wave staff arrays, *Mar. Freshwater Res.*, *49*, 89–101.

Babanin, A. V., and A. J. van der Westhuysen (2008), Physics of "saturation-based" dissipation functions proposed for wave forecast models, *J. Phys. Oceanogr.*, *38*, 1831–1841.

Babanin, A. V., and I. R. Young (2005), Two-phase behaviour of the spectral dissipation of wind waves, paper 51 presented at the Ocean Waves Measurement and Analysis, Fifth International Symposium, WAVES2005, Madrid.

Babanin, A. V., I. R. Young, and M. L. Banner (2001), Breaking probabilities for dominant surface waves on water of finite constant depth, *J. Geophys. Res.*, *106*(C6), 659–676.

Babanin, A. V., K. N. Tsagareli, I. R. Young, and D. Walker (2007), Implementation of new experimental input/dissipation terms for modeling spectral evolution of wind waves, paper presented at 10th International Workshop on Wave Hindcasting and Forecasting and Coastal Hazards, U.S. Army Eng. Res. and Dev. Cent. Coastal and Hydraul. Lab., Oahu, Hawaii.

Babanin, A. V., K. N. Tsagareli, I. R. Young, and D. J. Walker (2010a), Numerical investigation of spectral evolution of wind waves. Part II: Dissipation term and evolution tests, *J. Phys. Oceanogr.*, *40*, 667–683.

Babanin, A. V., D. Chalikov, I. R. Young, and I. Savelyev (2010b), Numerical and laboratory investigation of breaking of steep two-dimensional waves in deep water, *J. Fluid Mech.*, *644*, 433–463.

Banner, M. L., A. V. Babanin, and I. R. Young (2000), Breaking probability for dominant waves on the sea surface, *J. Phys. Oceanogr.*, *30*, 3145–3160.

Battjes, J. A., and J. Janssen (1978), Energy loss and set-up due to breaking of random waves, in *Proceedings of the 16th International Conference on Coastal Engineering*, pp. 569–588, Am. Soc. of Civ. Eng., Hamburg, Germany.

Booij, N., R. C. Ris, and L. H. Holthuijsen (1999), A third generation wave model for coastal regions: 1. Model description and validation, *J. Geophys. Res.*, *104*(C4), 7649–7666.

Bretherton, F. P., and C. J. R. Garret (1969), Wavetrains in inhomogeneous moving media, *Philos. Trans. R. Soc. London A*, *302*, 529–554.

Cardno (2007), Hydrodynamic and wave models calibration and validation, *Tech. Rep. RM2127*, Cardno Lawson Treloar, Camp Springs, Md.

Chawla, A., and J. T. Kirby (2002), Monochromatic and random wave breaking at blocking points, *J. Geophys. Res.*, *107*(C7), doi:10.1029/2001JC001042.

Dingemans, M. W. (1997), *Water Wave Propagation Over Uneven Bottoms: Linear Wave Propagation*, World Sci., Singapore.

Donelan, M., A. V. Babanin, I. R. Young, and M. L. Banner (2006), Wave-follower field measurements of the wind-input spectral function. Part II: Parameterization of the wind input, *J. Phys. Oceanogr.*, *36*, 1672–1689.

Eldeberky, Y. (1996), Nonlinear transformations of wave spectra in the nearshore zone, PhD thesis, 203 pp., Fac. of Civ. Eng., Delft Univ. of Technol., Netherlands.

Filipot, J.-F., and F. Ardhuin (2012), A unified spectral parameterization for wave breaking: From the deep ocean to the surf zone, *J. Geophys. Res.*, *117*, C00J08, doi:10.1029/2011JC007784.

Hasselmann, K. (1974), On the spectral dissipation of ocean waves due to white capping, *Boundary Layer Meteorol.*, *6*, 107–127.

Hasselmann, S., K. H. J. Allender, and T. Barnett (1985), Computation and parameterizations of the nonlinear energy transfer in a gravity-wave spectrum. Part II: Parameterizations of the nonlinear energy transfer for application in wave models, *J. Phys. Oceanogr.*, *15*, 1378–1391.

Huang, N. E., D. T. Chen, and C.-C. Tung (1972), Interactions between steady non-uniform currents and gravity waves with applications for current measurements, *J. Phys. Oceanogr.*, *2*, 420–431.

Hwang, P. A. (2011), A note on the ocean surface roughness spectrum, *J. Atmos. Oceanic Technol.*, *28*, 436–443.

Kirby, J. T., and T-M. Chen (1989), Surface waves on vertically sheared flows: Approximate dispersion relations, *J. Geophys. Res.*, *94*(C1), 1013–1027.

Komen, G. J., S. Hasselmann, and K. Hasselmann (1984), On the existence of a fully developed wind–sea spectrum, *J. Phys. Oceanogr.*, *14*, 1271–1285.

Kuik, A. J., G. Van Vleder, and L. H. Holthuijsen (1988), A method for the routine analysis of pitch-and-roll buoy wave data, *J. Phys. Oceanogr.*, *18*, 1020–1034.

Lai, R. J., S. R. Long, and N. E. Huang (1989), Laboratory studies of wave-current interaction: Kinematics of the strong interaction, *J. Geophys. Res.*, *94*(C11), 16,201–16,214.

Longuet-Higgins, M., and R. W. Stewart (1960), Changes in the form of short gravity waves on long waves and tidal currents, *J. Fluid Mech.*, *8*, 565–583.

Longuet-Higgins, M. S., and R. W. Stewart (1961), The changes in amplitude of short gravity waves on steady non-uniform currents, *J. Fluid Mech.*, *10*(4), 529–549.

Masson, D. (1996), A case study of wave-current interaction in a strong tidal current, *J. Phys. Oceanogr.*, *26*, 359–372.

Moreira, R. M., and D. H. Peregrine (2012), Nonlinear interactions between deep-water waves and currents, *J. Fluid Mech.*, *691*, 1–25.

Phillips, O. M. (1977), *The Dynamics of the Upper Ocean*, Cambridge Monographs on Mechanics and Applied Mathematics, 336 pp., Cambridge Univ. Press, London.

Phillips, O. M. (1984), On the response of short ocean wave components at a fixed wavenumber to ocean current variations, *J. Phys. Oceanogr.*, *14*, 1425–1433.

Pierson, W. J., and L. Moskowitz (1964), A proposed spectral form for fully developed wind seas based on the similarity theory of S. A. Kitaigorodskii, *J. Geophys. Res.*, *69*(24), 5181–5190.

Rapizo, H., A. Babanin, S. Aijaz, and K. Hessner (2015a), Wave modulation by tidal currents near Cook Strait, in *Proceedings of the Australasian Coasts and Ports Conference*, 6 pp., Auckland, New Zealand. [Available at http://search.informit.com.au/documentSummary;dn=724714914066501;res=IELENG.]

Rapizo, H., A. V. Babanin, E. Schulz, M. A. Hemer, and T. H. Durrant (2015b), Observation of wind-waves from a moored buoy in the Southern Ocean, *Ocean Dyn.*, *65*, 1275–1288.

Rapizo, H., T. Waseda, A. V. Babanin, and A. Toffoli (2016), Laboratory experiments on the effects of a variable current field on the spectral geometry of water waves, *J. Phys. Oceanogr.*, *46*, 2695–2717.

Ris, R. C., and L. H. Holthuijsen (1996), Spectral modelling of current induced wave-blocking, in *Proceedings of the 25th International Conference on Coastal Engineering*, pp. 1247–1254, Orlando, Fla. [Available at http://ascelibrary.org/doi/abs/10.1061/9780784402429.097.]

Rogers, W. E., A. V. Babanin, and D. W. Wang (2012), Observation-consistent input and whitecapping dissipation in a model for wind-generated surface waves: Description and simple calculations, *J. Atmos. Oceanic Technol.*, *29*, 1329–1346.

van der Westhuysen, A. J. (2012), Spectral modeling of wave dissipation on negative current gradients, *Coastal Eng.*, *68*, 17–30.

van der Westhuysen, A. J., M. Zijlema, and J. A. Battjes (2007), Nonlinear saturation-based whitecapping dissipation in swan for deep and shallow water, *Coastal Eng.*, *54*, 151–170.

van der Westhuysen, A. J., A. R. van Dongeren, J. Groeneweg, G. P. van Vledder, H. Peters, C. Gautier, and J. C. C. van Nieuwkoop (2012), Improvements in spectral wave modeling in tidal inlet seas, *J. Geophys. Res.*, *117*, C00J28, doi:10.1029/2011JC007837.

WAMDI Group (1988), The WAM model—A third generation ocean wave prediction model, *J. Phys. Oceanogr.*, *18*, 1775–1810.

Waseda, T., T. Kinoshita, L. Cavaleri, and A. Toffoli (2015), Third-order resonant wave interactions under the influence of background current fields, *J. Fluid Mech.*, *784*, 51–73, doi:10.1017/jfm.2015.578.

WL (2007), Evaluation and development of wave-current interaction in SWAN, *Tech. Rep. H4918.60*, Delft, Netherlands. [Available at http://repository.tudelft.nl/islandora/object/uuid%3A95be7960-1af2-4f5f-bb6d-37aed7e77ee9.]

Wolf, J., and D. Prandle (1999), Some observations of wave-current interaction, *Coastal Eng.*, *37*, 471–485.

Yan, L. (1987), An improved wind input source term for third generation ocean wave modelling, *Tech. Rep. 87–8*, The R. Netherlands Meteorol. Inst. (KNMI), Netherlands.